Traveling wave mode analysis of coherence collapse regime semiconductor laser with optical feedback

Mindaugas Radziunas[1], Deborah M. Kane[2]

submitted: July 19, 2024

[1] Weierstrass Institute
    Mohrenstraße 39
    10117 Berlin
    Germany
    E-Mail: Mindaugas.Radziunas@wias-berlin.de

[2] Research School of Physics
    Australian National University
    Canberra, ACT 2600
    Australia
    E-Mail: Deb.Kane@anu.edu.au

Traveling wave mode analysis of coherence collapse regime semiconductor laser with optical feedback

Mindaugas Radziunas, Deborah M. Kane

Abstract

A highly developed traveling wave model for a semiconductor laser system supports sophisticated mode analysis of the coherence collapse regime in semiconductor lasers with delayed optical feedback. The concept of instantaneous optical modes is used. Time-frequency representations of chaotic trajectories are constructed and interpreted from synthesizing the calculated optical modes with their corresponding steady states, analysis of the mode driving and coupling sources, and field expansion into modal components. The results support detailed physical interpretation of the optical and radiofrequency spectra in the coherence collapse regime.

1   Introduction

The system of a semiconductor laser (SL) with delayed optical feedback (DOF) from the external cavity (EC, see Fig. 1) has been researched extensively since the mid-1980s and was the subject of multiple reviews and monographs [1, 2, 3]. This system is an excellent example of nonlinear dynamics in general and nonlinear laser dynamics in particular. It was found that relatively small feedback from long ECs can cause chaotic operation of the SL. The chaotic laser emission has been researched for various applications, such as secure communication, random number generation, and reservoir computing [1, 2, 3, 4, 5]. Typically, these applications require chaotic emission with the radio frequency (rf) bandwidth reaching several to tens of GHz.
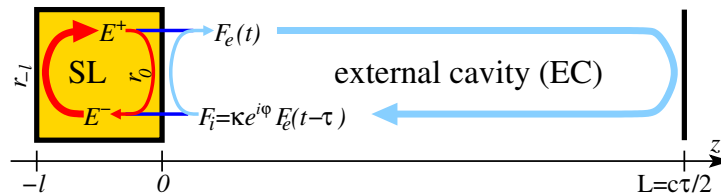

Figure 1: Schematic of a SLDOF, consisting of the SL and the EC.

Most theoretical studies of SLDOF systems are based on the Lang-Kobayashi (LK) model [6], a system of delay differential equations (DDEs) that assumes a single-mode operation of the SL, relies on the mean-field approximation and models the impact of DOF by the (in general-complex) feedback *rate* η. For Fabry-Perot (FP) lasers, $\eta = \frac{1-|r_0|^2}{r_0\tau_0}\kappa e^{i\varphi}$, where $\tau_0 = 2ln_{\mathrm{g}}/c$ is the field roundtrip time in the SL and r_0 is its complex amplitude reflectance at the front facet $z = 0$ (l: SL length, c: speed of light in vacuum, n_{g}: group velocity factor in the SL). κ is the fraction of the emitted optical field amplitude that is reinjected, and φ is the frequency-independent field phase shift within the EC. φ plays a crucial role when considering millimeter length ECs [7, 8]. It can be neglected for long delays $\tau = 2L/c$ (L: effective length of the EC) used in most experimental free space propagation SLDOF systems. Despite the simplicity, the LK model and its further developments predict much of the experimentally observed complex behavior [9, 10]. In particular, the coherence collapse (CC) [11], which is the sudden feedback-induced transition from single-frequency operation to a chaotic output, and low-frequency fluctuation (LFF), a phenomenon that modulates the chaotic state. In many cases, the underlying dynamics in the SLDOF could be understood from calculations and analysis of the steady states in

the LK- and related DDE systems. In SLDOF systems with moderate and large τ, the number of these steady states, best known as the *external cavity modes* (ECMs), can be huge, and most, if not all of them, are unstable. Stable and unstable manifolds of many of these ECMs play a decisive role in the chaotic attractor, see, e.g., Refs. [12, 13, 14, 15], where the role of ECMs in defining the CC and LFFs was revealed.

However, the LK model has its drawbacks. It ignores the presence of multiple longitudinal modes (resonances) in the solitary laser, is restricted to low feedback levels, and is not suited for modeling SLDOF systems with small or vanishing front facet reflectance r_0 of the FP SL. In contrast, the traveling wave (TW) model [16, 17], which is a system of partial differential equations (PDEs) in time and one spatial direction along the SL and EC, extends to arbitrarily high optical feedback levels and naturally accounts for spatial distributions of fields and carriers, field reflections at the SL facets, and multiple longitudinal modes of a solitary SL. In the present work, we calculate and analyze the steady states and *instantaneous* optical modes of the TW model [7, 16, 18] for the SLDOF operating in the CC regime. It is shown that mode analysis can provide information comparable to that obtained when analyzing the ECMs of the LK model [15]. This applies even with the TW model extensions which are outside the scope of the LK model (e.g., accounting for spatial distributions of fields and carriers within the SL), or when using model parameters where the LK model is not trustworthy. The field expansion into optical modes provides a correct time-frequency domain representation of the field transients and allows analyzing the formation of simultaneously operating large-amplitude modes or mode clusters. These are responsible for specific mode-beating oscillations visible in the rf spectrum. In contrast to previously analyzed short SL devices [7, 18], where only a few or a few tens of instantaneous modes were of importance, now we trace the evolution of more than a thousand modes, many of which contribute to the chaotic dynamics of the SLDOF.

2 Model

2.1 Traveling wave model

The TW model is based on equations for the complex, slowly varying counter-propagating optical fields $E^+(z, t)$ and $E^-(z, t)$ in the FP laser ($z \in [-l, 0]$):

$$
\begin{cases}
\left(\frac{n_g}{c}\partial_t \pm \partial_z\right)E^{\pm}(z,t) = -i\big[\beta(z,t) - i\mathcal{D}\big]E^{\pm}(z,t) + F^{\pm}_{\mathrm{sp}}, \\
F_e(t) = \sqrt{1 - |r_0|^2}\, E^+(0,t) - r_0^* F_i(t) \\
E^-(0,t) = \sqrt{1 - |r_0|^2}\, F_i(t) + r_0 E^+(0,t) \\
F_i(t) = \kappa e^{i\varphi} F_e(t - \tau), \quad E^+(-l,t) = -r^*_{-l}E^-(-l,t).
\end{cases}
\tag{1}
$$

Here, $F^{\pm}_{\mathrm{sp}}$ represent Langevin noise sources, F_e and F_i are the EC-side SL-emitted and reinjected optical fields, respectively. r_{-l} is the field amplitude reflectance at the rear SL facet, $z = -l$. By normalization, $|E(z,t))|^2 = |E^+|^2 + |E^-|^2$ is the local photon density. $\mathcal{D}$ is a linear operator describing Lorentzian-shaped material gain dispersion [16]

$$
\mathcal{D}E^{\pm} = \frac{\bar{g}}{2}(E^{\pm} - p^{\pm}), \quad \frac{\lambda_0^2}{2\pi c}\frac{d}{dt}p^{\pm} = \frac{\bar{\gamma}}{2}(E^{\pm} - p^{\pm}) - i\bar{\lambda}p^{\pm},
\tag{2}
$$

where $\bar{g}$, $\bar{\gamma}$, and $\bar{\lambda}$ represent the height, full width at half maximum, and detuning of the material gain peak from the central wavelength λ_0, respectively. $p^+(z,t)$ and $p^-(z,t)$ are the complex polarization functions. $\beta(z,t)$ is the z-dependent complex field propagation factor,

$$
\beta(z,t) = i\frac{g_T - \alpha_0}{2} - \frac{\alpha_H g'(N(z,t) - N_{\mathrm{tr}})}{2}, \quad g_T = \frac{g'(N(z,t) - N_{\mathrm{tr}})}{1 + \varepsilon P(z,t)},
\tag{3}
$$

which depends on the carrier density N and, through the total gain function g_T, photon density P. α_0, g', N_{tr}, ε, and α_{H} are field losses, differential gain, transparency carrier density, nonlinear gain compression, and linewidth enhancement factor, respectively. Evolution of N is defined by the rate equation [16],

$$\frac{d}{dt}N(z,t) = \frac{I}{qV} + \frac{U_F'}{qVR_s}(\langle N \rangle - N) - \frac{N}{\tau_N} \\ - \frac{c}{n_g}\Re \sum_{\nu=\pm} E^{\nu *} \cdot \big(g_T(N,P) - 2\mathcal{D}\big)E^\nu, \tag{4}$$

where $P(z,t) = |E(z,t)|^2$, $\langle \rangle$ denotes the spatial average over the SL, q is the electron charge, while parameters V, τ_N, I, R_s, and U_F' are the volume of the active region, carrier lifetime, injection current, series resistance, and derivative of the Fermi level separation, respectively. In our calculations presented along this paper, if not stated differently, we use $\lambda_0 = 830\,\text{nm}$, $\tau = 4.5\,\text{ns}$, $\varphi = 0$, $l = 300\,\mu\text{m}$, $r_0 = (0.05)^{1/2}$, $r_{-l} = (0.95)^{1/2}$, $n_g = 3.7$, $g' = 1.036 \cdot 10^{-20}\,\text{m}^2$, $N_{\text{tr}} = 10^{24}\,\text{m}^{-3}$, $\alpha_0 = 60\,\text{cm}^{-1}$, $V = 300\,\mu\text{m} \times 5\,\mu\text{m} \times 0.1\,\mu\text{m}$, $\tau_N = 2\,\text{ns}$, $\bar{\lambda} = 0\,\text{nm}$, $\bar{\gamma} = 30\,\text{nm}$, $\bar{g} = 100\,\text{cm}^{-1}$, $R_s = 1\,\Omega$, $U_F' = 3.5 \cdot 10^{-26}\,\text{Vm}^3$, $I = 55\,\text{mA}$ (about 2.2 times the threshold current $I_{\text{th}} \approx 25\,\text{mA}$), $\kappa = 0.1$, $\alpha_{\text{H}} = 3.5$, and $\varepsilon = 3 \cdot 10^{-23}\,\text{m}^3$. All these parameters (except for the Lorentzian dispersion width, which is halved in the present paper) were used in Ref. [19]. Most of them were translated from Ref. [20]. They are estimates which connect with a commercial SL for which there is comprehensive experimental data [21, 22].

2.2 Example

The TW model with the parameter set introduced above was used to simulate changes in the SLDOF dynamics with a step-wise increase of the feedback factor $\kappa \in [0, 0.32]$. For each fixed κ, we calculated $1.5\,\mu\text{s}$-long transients, evaluated the dynamical states using the last $1\,\mu\text{s}$ of these transients, and increased κ by 0.001 afterward. Fig. 2 represents these parameter continuation simulations. The spectral mappings in panels (a) and (b) show the power of the rf and optical spectra as functions of κ in $[0, 53]$ GHz rf- and $[-0.16, 0.35]$ nm relative wavelength domains. These (time-averaged) spectra were obtained by applying the discrete fast Fourier transform (DFFT) to the time traces of the emitted field intensity $|F_e(t)|^2$ and its complex amplitude $F_e(t)$, respectively. Due to the vast number of field values in the discrete time trace, optical spectra were estimated in 32 non-overlapping time subintervals covering the whole $1\,\mu\text{s}$ time range and averaged afterward. The considered rf domain in panel (a) represents an experimentally accessible part of the entire rf spectrum; the spectral peaks at about 135 GHz (corresponding to the solitary SL resonance separation) and further harmonics for a few selected κ are shown in panel (c) (note the logarithmic scale of the abscissa-axis there). The wavelength range of panel (b) comprises two central solitary SL resonances; an extended representation of the optical spectra involving six SL resonances separated by about 0.31 nm, at several values of κ is given in panel (d). Panels (a) and (b) show several well-known regimes of the SLDOF system [9, 10]. In region A at $\kappa \lesssim 0.01$, the device operation is determined by the solitary SL, whereas the feedback is just a small perturbation. The broad rf spectra and broadened peaks of optical spectra around each SL resonance characterize the chaotic CC regime (region B). To the left- and right from $\kappa \approx 0.07$, we can also distinguish the regimes without and with strong LFFs (regions B' and B''), the latter represented by the high-intensity spectral peak at the bottom of the panel (a). Since we simulated well above the threshold operating laser, $I/I_{\text{th}} \approx 2.2$, the initial evidence of LFFs is observed at already enhanced feedback values, which is consistent with [23]. In contrast to the widely investigated LFFs in SLs operating close to the lasing threshold, the simulated LFF events in this work do not exhibit well-distinguishable emission intensity drops (which can be measured in experiments). Instead, they can be recognized by a sudden rise in $\langle N \rangle$ to levels typical for solitary SL lasing and operation at these levels for a time interval of approximately τ. The frequency of LFFs decays with the increase of
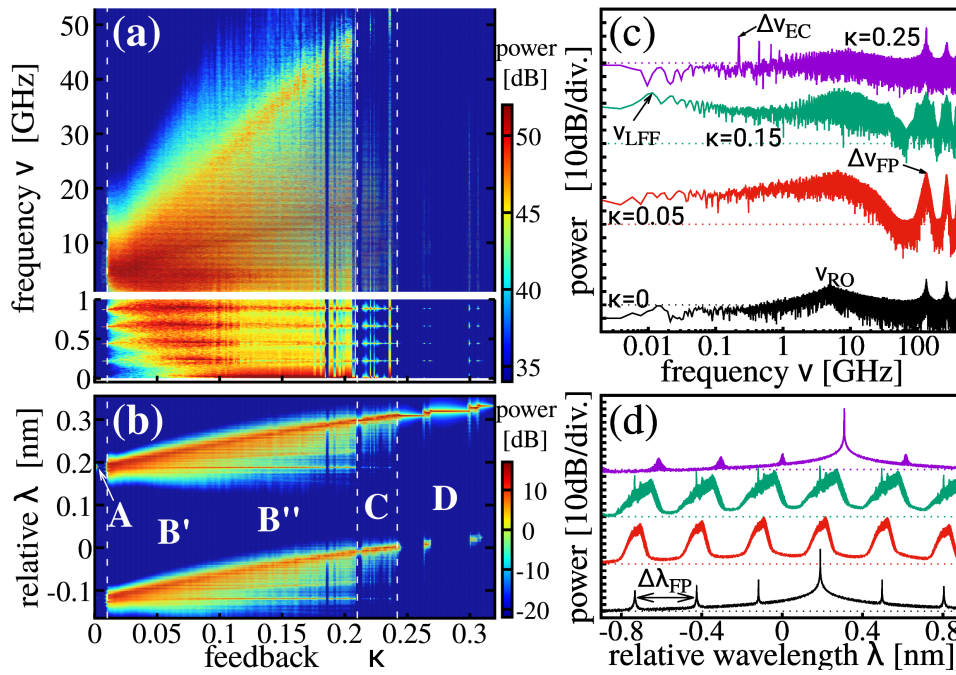
Figure 2: Rf (a) and optical spectrum (b) mappings for increased κ, color-coded on a dB scale. (c), (d): spectra for $\kappa = 0$ (black), 0.05 (red), 0.15 (green), and 0.25 (magenta) in extended rf- and wavelength ranges. Dotted horizontal lines: background levels (20 dB in (c) and -50 dB in (d)) of each spectrum. Note different frequency scalings in upper and lower parts of (a).

κ, such that these LFF events can remain undetected for $\kappa \gtrsim 0.18$ and limited transient lengths. For $\kappa \gtrsim 0.24$, region D, we have a relatively regular (sometimes-transient) regime with low intensity of the rf spectra, small-amplitude fluctuations of N, and operation of a single or only a few optical modes red-shifted by about 0.1 nm from one or several solitary SL resonances. κ-induced switching between the small- and moderate-intensity rf spectra here are mainly related to transitions between the steady states with almost the same threshold densities. Finally, intermediate region C contains spectra similar to those typical for regions B" and D. The observed switchings between different spectra can be due to insufficiently long transients or bistability reported in Ref. [15]. The rf and optical spectra of typical representatives of regimes A, B', B", and D are shown in panels (c) and (d). The spectra are up-shifted, and horizontal dotted lines indicate the same background level of the corresponding spectrum. For $\kappa = 0$ (black) and $\kappa = 0.25$ (magenta), we have regular steady-state regimes (the rf intensity is low, and peaks of optical spectra are narrow). For $\kappa = 0.05$ (red) and $\kappa = 0.15$ (green), we have the CC without and with LFF. The rf spectra, panel (c), have enhanced intensity over several tens of GHz and a high LFF component at about 0.01 GHz when $\kappa = 0.15$. At the same time, the optical spectra around each SL resonance are broadened, see panel (d). By analyzing well-pronounced spectral peaks, we recognize the solitary FP SL induced $\Delta\lambda_{FP} \approx 0.31$ nm separated resonances in (b), (d) and corresponding $\Delta\nu_{FP} \approx 135$ GHz beat frequencies and higher harmonics in (c). The horizontal high-intensity stripes in (a), spaced by $\Delta\nu_{EC} = 1/\tau \approx 0.22$ GHz, represent the mixing of the EC roundtrip (or ECM separation) induced beat frequency in the nonlinear model for the SLDOF. The undamped relaxation oscillations (ROs), which are mainly due to the nonlinear interaction of fast optical fields and slow carriers, are represented by high-intensity values of the rf spectra at $\nu_{RO} \approx 4$-to-5 GHz in (a) and by the corresponding spectral peak separation close to the solitary SL resonances at the onset of the CC in (b). ν_{RO}, which can be efficiently changed by tuning the bias current I, also depends on other model parameters, including the feedback factor κ. Other prominent peaks of the rf

spectra in (a) and corresponding optical spectra in (b) can hardly be explained without performing a more detailed analysis of the optical modes of the TW model, which is the main topic of the present paper.

2.3 Mode analysis

Besides the numerical integration of the TW model equations and the study of the calculated transients, we can perform a nontrivial analysis of model equations and calculated states based on the *instantaneous* optical modes, pairs $[\Theta(z), \Omega]$ of complex vector-function $\Theta = \begin{pmatrix} \Theta^+ \\ \Theta^- \end{pmatrix}$ and frequency Ω, both depending on the instant distribution $\beta(z, t')$ [7]. To find these modes at any fixed $\beta(z)$, we substitute the Ansatz $\Psi(z, t) = \begin{pmatrix} E^+ \\ E^- \end{pmatrix} = e^{i\Omega_j t} \Theta_j(z)$ into Eq. (1) and resolve the resulting spectral problem. Real and imaginary parts of Ω_j, $\Re\Omega_j$ and $\Im\Omega_j$, are optical frequency (relative to the central frequency $\omega_0 = \frac{2\pi c}{\lambda_0}$) and damping of the mode, respectively. The condition $\Im\Omega_j = 0$, together with the balance of the carrier rate equation within the SL, is used to find the steady states [18] of the TW model defined in the spatially extended compound cavity consisting of the SL and EC. These steady states, also referred to as *compound cavity modes* (CCMs), typically can be well represented by the optical frequency ω_s and the threshold carrier density N_s (or its spatial average $\langle N_s \rangle$) [16, 18]. They are TW model analogs of the ECMs of the LK model. The state with the smallest threshold N_s is known as a maximal gain mode (MGM) in the LK and TW models.

Next, we can decompose calculated function $\Psi(z, t)$ into a series of mode functions calculated for actual $\beta(z, t)$ [7],

$$\Psi(z, t) = \sum_j f_j(t)\Theta_j(z; \beta(z, t)), \qquad f_j(t) = \frac{(\Theta_j^\dagger, \Psi(z, t))}{(\Theta_j^\dagger, \Theta_j)},$$
$$(\xi, \zeta) = n_g \int_{-l}^0 \xi^{*T}(z)\zeta(z)dz + \int_0^L \xi^{*T}(z)\zeta(z)dz. \tag{5}$$

After scaling the modes such that $\Theta_j^+(0^+; \beta) = 1$ (0^+: EC edge at the front SL facet), complex mode amplitudes $f_j(t)$ show mode contributions to SL emission at the EC side, $F_e(t) = \sum_j f_j(t)$. $(\cdot, \cdot)$ brackets in (5) denote a scalar product of complex vector functions, accounting for different field velocities in the SL and EC. For reconstruction of $\{\Theta_j\}$ and Ψ in the EC, we explore field equations in (1) for $z \in [0, L]$, assuming $n_g = 1$, $F_{sp} = \mathcal{D} = 0$, and constant β_{EC}, $e^{-i2\beta_{EC}L} = \kappa e^{i\varphi}$, which models uniformly along the EC distributed attenuation and phase shift and assumes a perfect field reflection at the mirror of the EC. Modes are not orthogonal in the sense of the scalar product. To find $f_j(t)$ in Eq. (5), we construct the adjoint spectral problem [7, 8], define adjoint modes $[\Theta_j^\dagger(z), \Omega_j^*]^1$, and explore the orthogonality relation $(\Theta_k^\dagger, \Theta_l) = 0$ when $\Omega_k \neq \Omega_l$. Besides providing valuable information on the contribution of different modes to calculated emission, the mode expansion (5) can also be used to approximate field equations (1) with a system of ODEs for mode amplitudes. Namely, by substituting Eq. (5) into Eq. (1) and accounting for (slow) changes of β, we can derive the system [7, 8]

$$\frac{d}{dt}f_k(t) = i\Omega_k f_k - \sum_l K_{k,l}(\beta)f_l + \zeta_{sp}^{(k)},$$
$$K_{k,l} = \frac{(\Theta_k^\dagger, \frac{d}{dt}\Theta_l)}{(\Theta_k^\dagger, \Theta_k)}, \quad \zeta_{sp}^{(k)} = \frac{(\Theta_k^\dagger, F_{sp})}{(\Theta_k^\dagger, \Theta_k)}, \tag{6}$$

which can explain the evolution and coupling of different mode amplitudes. These equations show that steady-states with vanishing $|\frac{df}{dt}|$ and $\frac{d\Theta}{dt}$ (thus, $K_{k,l}$) should have $\Im\Omega = 0$. On the other hand, when β is changing in time, each f_k, even with $\Im\Omega_k > 0$, can be excited not only by the noise term $\zeta_{sp}^{(k)}$ but also by (typically small) coupling to other modes with nonvanishing f_l. Following Ref. [8], one can show

---

[1] $\Theta_j^\dagger(z)$ can be easily constructed by exchanging and complex conjugating the first and second components of $\Theta_j(z)$.

that the complex mode coupling terms in Eq. (6) are proportional to $\frac{dN}{dt}$ (which is small since carriers are slow) and inversely proportional to the mode separation $\Omega_k - \Omega_l$ [8], such that the direct coupling of distant modes is small. Notably, the mode coupling $K_{k,l}$ and the self-coupling $K_{k,k}$ in the dynamical state still can be significant since they are also proportional to Petermann's factor $\sqrt{K_z} = \frac{(\Theta_k, \Theta_k)}{|(\Theta_k^\dagger, \Theta_k)|}$ [24], which turns to infinity at the mode degeneracy [25] (also known as the exceptional point, EP [26]), where $(\Theta_k^\dagger, \Theta_k) \rightarrow 0$.[2] Thus, the evolution of mode amplitudes in the vicinity of the EP is defined not only by Ω but also by the significant coupling to the neighboring modes. Depending on the phase of complex coupling and self-coupling coefficients and the phase difference of the involved mode amplitudes, the mode coupling terms can significantly contribute to the growth or decay of mode amplitudes: see, e.g., Ref. [7], where our mode analysis revealed a crucial role of the mode with ever positive $\Im\Omega$ in defining the shape of the dispersive-Q-switching pulses in multisection SLs.

3   Modes in the simplified model

For a simplified TW model with a spatially averaged carrier rate equation (i.e., $N \equiv \langle N \rangle$), neglected gain compression ($\varepsilon = 0$) and dispersion ($\mathcal{D} = 0$), the factor $\beta = \beta(N)$ is a complex number, and the mode-defining equation for the SLDOF reads as

$$\frac{\mathcal{G}(N,\Omega)+1}{\mathcal{G}(N,\Omega)+|r_0|^2} = -\frac{\kappa e^{i(\varphi-\Omega\tau)}}{r_0}, \qquad \mathcal{G} \overset{def}{=} r_{-l}^* r_0 e^{-i(2\beta(N)l+\Omega\tau_0)}. \tag{7}$$

When $\kappa = 0$, the condition $\mathcal{G}(N_{\mathrm{FP}}, \omega_{\mathrm{FP}}) = -1$ following from Eq. (7) defines resonances (threshold density and real optical frequency) of the solitary SL. Eq. (7) is a single complex equation relating *real* number N and *complex* Ω, i.e., determines multiple *mode branches* in 3-dimensional ($\Re\Omega/\Im\Omega/N$) space. Eq. (7) can be used for finding threshold density N_s and real frequency ω_s of the CCMs (having $\Im\Omega = 0$) or searching branches of N-dependent complex mode frequencies $\Omega(N)$.

3.1   Compound cavity modes

For the CCM-location problem ($\Im\Omega = 0$, s.t. $\Omega = \omega$ is real), an elimination of the feedback phase φ from Eq. (7) implies

$$\Delta\omega = \frac{\alpha_{\mathrm{H}} g' l}{\tau_0} \Delta N \pm \frac{1}{2} W(\Delta N), \qquad \text{where}$$
$$\Delta\omega = \Re\Delta\Omega \overset{def}{=} \Omega - \omega_{\mathrm{FP}}, \quad \Delta N \overset{def}{=} N - N_{\mathrm{FP}}, \tag{8}$$
$$W(\Delta N) = \frac{2}{\tau_0} \arccos \frac{\cosh(g'l\Delta N) - \kappa^2 \cosh(g'l\Delta N - \ln|r_0|^2)}{1-\kappa^2}.$$

This relation defines φ-parametrized CCM branches in a (real) frequency- and carrier density offset ($\Delta\omega/\Delta N$) domain, see Fig. 3. These branches are analogs of the ECM ellipses in the LK model. $\Delta\omega = \frac{\alpha_{\mathrm{H}} g' l}{\tau_0} \Delta N$ defines the diagonal of the branch, and $W(\Delta N)$ is its width at fixed ΔN. In contrast to the LK model, the TW model defines CCM branches in the neighborhood of all solitary SL resonances, empty bullets in Fig. 3(a). For small κ, closed CCM loops are in nearly perfect agreement with the corresponding ever-regular ECM ellipses of the LK model. With the increasing κ, these loops

---

[2]The concept of mode degeneracy, i.e., the parameter space singularities where two modes have the same eigenvalue, was introduced in Ref. [25] in the context of self-pulsating multisection SLs. It was shown later, see, e.g., [7, 27] and references therein, that this EP plays a crucial role in defining various dynamical states of multisection lasers. Finding the EP in more advanced models for SLDOF and its role in determining the dynamics, particularly properties of the coherence collapse state, requires more detailed analysis and will be discussed elsewhere.

asymmetrically grow until the neighboring loops collide at $\kappa = |r_0|$ and $\Delta N \to \infty$ and form a single curve, bypassing from below all solitary SL resonances afterward. To determine CCMs on the fixed-κ branches, one has to find points corresponding to the predefined value of φ. For the considered SLDOF, the CCMs are densely packed on each such curve. For example, each thick red loop in Fig. 3(a) and (b), calculated for $\kappa = 0.1$, accommodates about 640 CCMs almost equally spaced by the cavity roundtrip frequency $(\tau + \tau_0)^{-1}$.
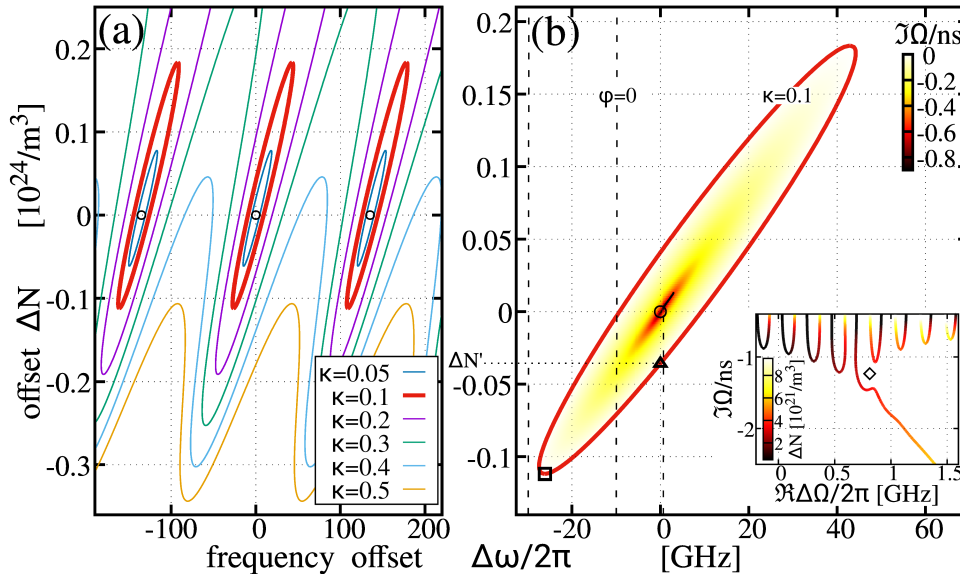

Figure 3: Modes of the simplified TW model with $\varepsilon = \mathcal{D} = 0$, $N = \langle N \rangle$ in frequency/carrier density offset domain. (a): CCMs for several fixed κ and arbitrary φ. Empty bullets: solitary SL resonances. (b): Same representation close to one of these resonances for $\kappa = 0.1$ (red curve). Black triangle and box: CCM $(0, \Delta N')$ and MGM. Vertical dashed lines: $\Re\Delta\Omega_j$ of three selected modes. Shading: (negative) damping $\Im\Omega_j(N)$ of all modes. Inset: traces of a few complex $\Omega(N)$ with growing N (from black to yellow) near the EP (empty rhomb).

All but one CCM (ω_s, N_s) on the lower part of closed loops ["node", or "mode" in the LK system] surrounding the FP resonances has a dual CCM $(\omega_s^\star, N_s^\star)$ ["saddle" or "antimode"] with $\omega_s^\star \approx \omega_s$ and $N_s^\star > N_s$ on the upper part of the same loop. The CCM pair can merge (or be generated) in a saddle-node bifurcation close to vertical borders of each curve. CCM pairs are defined by a single mode, which has $\Im\Omega = 0$ and fulfills Eq. (7) at two different values of N. The mode-antimode pair separation, $N_s^\star - N_s$, can be approximated by the CCM curve height $H(\Delta\omega_s)$ at the corresponding frequency offset $\Delta\omega_s$. When defined, it is a function of model parameters, and it increases with an increase of κ. In contrast to the LK model, it becomes undefined when κ significantly exceeds $|r_0|$; see, e.g., the mustard ($\kappa = 0.5$) curve in Fig. 3(a), where dual "antimodes" do not exist.

When a stable single-mode lasing of the SLDOF is possible, it is determined by or is close to the MGM having the smallest possible ΔN_s. Since the CCM separation of the considered SLDOF is small, the MGM's position is well approximated by the lower border of the corresponding CCM curve, see black box in Fig. 3(b), where $W(\Delta N) = 0$ and, thus,

$$\Delta N_{\mathrm{MGM}} = \frac{\tau_0 \Delta\omega_{\mathrm{MGM}}}{\alpha_{\mathrm{H}} g' l}, \quad \Delta\omega_{\mathrm{MGM}} = -\frac{\alpha_{\mathrm{H}}}{\tau_0} \ln\left(\frac{1 + \kappa/|r_0|}{1 + \kappa|r_0|}\right). \tag{9}$$

Knowledge of $\Delta\omega_{MGM}$ helps to understand and estimate the chaotic operation bandwidth and predict shifts of the dominating peaks in the optical spectrum with the change of κ. The carrier offset $\Delta N'$ of

another important CCM located just below the solitary SL resonance, as indicated by the black triangle at $(0, \Delta N')$ in Fig. 3(b), can be determined by solving

$$\frac{\alpha_{\mathrm{H}} g' l}{\tau_0} \Delta N' + \frac{1}{2} W(\Delta N') = 0. \tag{10}$$

The half-width of the CCM branch, $\frac{1}{2} W(\Delta N')$, will be used later to explain the positions of prominent peaks in the rf spectrum.

In the LK model, all formulas presented above admit analytic expressions, which are in perfect agreement with the TW model-induced formulas when optical feedback is small.

3.2 Mode amplification and damping

In a dynamic state, such as the CC, one expects contributions from several modes due to the fluctuation of N. The modes with $(\Re\Omega, N)$ inside the CCM loop corresponding to the applied κ or above the continuous curve, if $\kappa \geq |r_0|$, have negative damping, $\Im\Omega < 0$. The presence of CCMs within a specific frequency range is directly related to the existence of the modes capable of achieving negative $\Im\Omega$ and being amplified when N exceeds the mode threshold N_s. However, only a few such modes can typically be accessed and amplified. If the time-varying ΔN does not exceed the level of, e.g., $\Delta N'$, see horizontal thin dotted line in Fig. 3(b), only the modes with $\Re\Delta\Omega \in [\Delta\omega_{\mathrm{MGM}}, 0]$ near the analyzed solitary SL resonance can attain negative $\Im\Omega$. Due to typically small mode coupling factors $K_{k,l}$ in Eq. (6), the noise factor $\zeta_{\mathrm{sp}}^{(k)}$ is the only gain source for all remaining modes.

Colored shading inside the CCM loop in Fig. 3(b) calculated for $\kappa = 0.1$ represents the negative damping of modes at the corresponding value of $N = N_{\mathrm{FP}} + \Delta N$. Each mode can reach its own smallest (largest negative) $\Im\Omega$ when its $(\Re\Omega, N)$ is located on the diagonal line of the loop. The overall largest negative $\Im\Omega$ is reached close to the solitary SL resonance; see dark red-to-black shading around the empty black bullet in Fig. 3(b). When increasing N, real frequencies $\Re\Omega(N)$ of all but one mode near each SL resonance show only moderate changes, which do not exceed the CCM separation frequency; see the two leftmost vertical dashed lines in Fig. 3(b) representing two selected mode branches $\Omega(N)$. The mode branch with $\Re\Delta\Omega/2\pi \approx -10\,\mathrm{GHz}$ can have both positive and negative $\Im\Omega(N)$ and determines two CCMs ($\Im\Omega(N) = 0$) at the crossings with the red loop. The branch with $\Re\Delta\Omega/2\pi \approx -30\,\mathrm{GHz}$ is outside of this loop and has only positive $\Im\Omega$. The exceptional mode (dashed line with $\Re\Delta\Omega \approx 0$) determines a single CCM and also shows only small frequency changes and a moderate decrease of $\Im\Omega$ for negative ΔN. However, once ΔN exceeds some critical positive value (which is about $5 \cdot 10^{21}\,\mathrm{m}^{-3}$ in our case), the path of the mode turns right and follows the diagonal of the CCM loop. At the same time, $\Im\Delta\Omega$ of this exceptional mode continues decreasing: see brown-to-black dash within the red-shaded area close to the SL resonance in Fig. 3(b). Since $\Im\Delta\Omega$ enters the argument of the exponential function, the numerical continuation of the path of the mode could be performed only up to $\Im\Delta\Omega \approx -10/\mathrm{ns}$.

Branches of a few modes with the largest negative $\Im\Omega$ close to the SL resonance are presented in the inset of Fig. 3(b). Different colors represent the changing value of ΔN used for mode calculations. The minimal $\Im\Omega$ (turning points of mode branches) and the largest $\Re\Omega$-shifts of all but the exceptional mode are achieved at $(\Re\Delta\Omega, \Delta N)$ belonging to the diagonal of the CCM loop. The exceptional mode, however, bypasses close in the parameter space located EP [25, 26], see black rhomb in the inset, and exhibits a further nearly linear with ΔN decrease of $\Im\Omega$ and increase of $\Re\Omega$. The positions $(\Re\Omega, N)$ and $\Im\Omega$ of the EP also depend on the feedback factor κ and other model parameters. For example, comparing to the values presented in Fig. 3(b) and its inset, $\Im\Omega$ of the close-to-the-EP-modes and $\Im\Omega_{\mathrm{EP}}$ of the EP itself can reach larger negative values with increased κ. On the other hand, $\Im\Omega_{\mathrm{EP}}$

vanishes when $\kappa \approx 3.86 \cdot 10^{-4}$. For the location of the EP in the above-discussed simplified TW model, i.e. finding of $(N_{\mathrm{EP}}, \Omega_{\mathrm{EP}})$, and the specific value of one of the model parameters, e.g., φ_{EP}, one has to resolve Eq. (7) together with an additional complex equation

$$\mathcal{E}(N, \Omega) \overset{def}{=} 1 + \frac{\tau}{\tau_0} \frac{(\mathcal{G}(N,\Omega)+|r_0|^2)(\mathcal{G}(N,\Omega)+1)}{(1-|r_0|^2)\mathcal{G}(N,\Omega)} = 0. \tag{11}$$

In the example of Fig. 3, the value of φ_{EP} was different from $\varphi = 0$ used in the mode branch calculations. Thus, a fine-tuning of φ, which implies smooth shifts of (almost all) CCMs and mode branches [7, 16, 18], will also cause the situation where two mode branches in the inset of Fig. 3(b) hit the EP at $N = N_{\mathrm{EP}}$ and exchange their tails for $N > N_{\mathrm{EP}}$ with a further tuning of φ. Notably, since $(\Theta^\dagger, \Theta) \propto \mathcal{E}(N, \Omega)$, the factors $K_{k,k}$ and $K_{k,l}$ in Eq. (6) and $\sqrt{K_z}$ of the k-th mode, being inversely proportional to $(\Theta_k^\dagger, \Theta_k)$, can become very large near the EP.

4   Modes in the general TW model

In Fig. 3 and the discussion above, we explored the simplest version of the TW model. If gain dispersion is nonvanishing, $\mathcal{D} \neq 0$, Eqs. (7) and (8) are more involved, and finding the CCM branches in Fig. 3 requires exploration of numerical continuation procedures. The main difference in the mode landscape is the up-shift of the CCM curves toward higher N with the increasing distance from the gain peak frequency. However, simple relations (8) used for finding the CCMs in the simplified TW
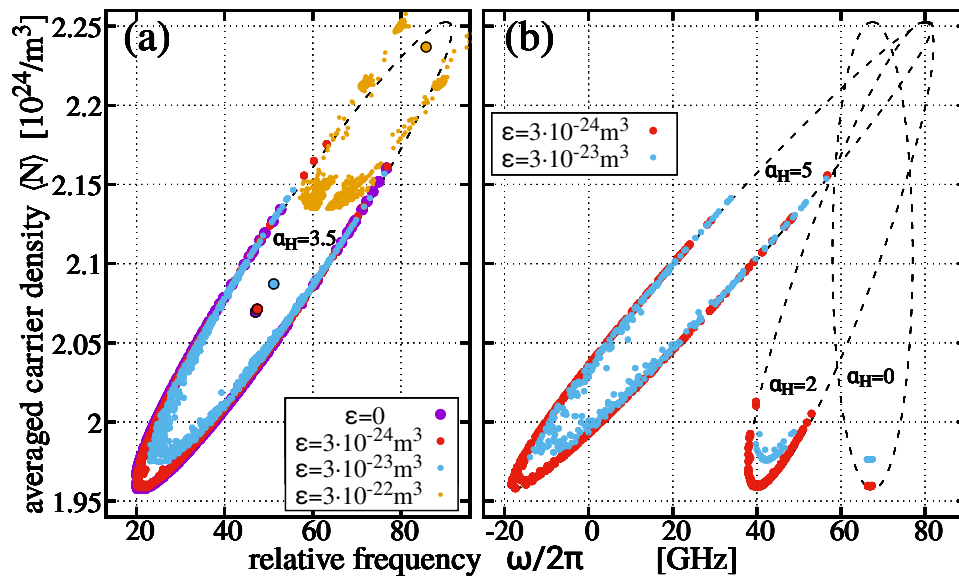

Figure 4: Modes with $\Im\Omega \approx 0$ detected during simulations of the general TW model (dots) and CCM loops (dashed) in the simplified TW model, see also Fig. 3, in frequency/spatially averaged carrier density domain. (a): $\alpha_{\mathrm{H}} = 3.5$ and $\varepsilon = 0$ (magenta), $3 \cdot 10^{-24}$ m^3 (red), $3 \cdot 10^{-23}$ m^3 (light blue), and $3 \cdot 10^{-22}$ m^3 (mustard). Black framed bullets: solitary SL resonances. (b): $\varepsilon = 3 \cdot 10^{-24}$ m^3 (red) and $3 \cdot 10^{-23}$ m^3 (light blue), whereas $\alpha_{\mathrm{H}} = 0, 2$, and 5, as indicated in the corresponding loops.

model do not work when assuming spatially distributed $N(z)$ and, thus, $\beta(z)$. The methods for locating the steady states are much more involved, requiring finding the steady-in-time spatially distributed function $N_s(z)$ instead of a simple constant N_s [18]. The algorithms of Ref. [18] were used to calculate the steady states of the solitary SL; see black-framed bullets in Fig. 4(a).

Fortunately, the complexity of mode calculations using the provided spatially distributed β is nearly the same as in the constant β case. Thus, besides drawing analytically available CCM curves of the simplified TW model, dashed curves in Fig. 4, we can also collect positions in the $\omega/\langle N \rangle$ plane where $\Im\Omega$ of the corresponding calculated mode vanishes or is very close to zero. The distributions $\beta(z)$ used in mode calculations were collected from 100 ns-long transient simulations of the general TW model, using about 25 ps steps before recalculating the modes. For a better approximation of the CCM curve, simulations of the states with large amplitude variations of $\langle N \rangle$ (a LFF state, for example) are preferable. We have found that once the gain compression is neglected, $\varepsilon = 0$, previously calculated CCM curves perfectly agree with the recorded zero-$\Im\Omega$ positions: c.f. dashed loop and magenta dots in Fig. 4(a). The dots do not cover the upper part of the dashed loop since the corresponding values of $\langle N \rangle$ are not reached during the simulations. An introduction of only small gain compression, $\varepsilon = 3 \cdot 10^{-24}$ m^3 (red dots in Fig. 4), implies only a slightly increased scatter and a small up-shift of the zero-$\Im\Omega$ positions along the diagonal of the CCM loop. Since the solitary SL resonance is up-shifted along the loop's diagonal as well, our theoretical estimates (8), (9) still can provide decent approximations of corresponding quantities in general TW model even for a ten-fold higher gain compression, $\varepsilon = 3 \cdot 10^{-23}$ m^3 (light blue dots in Fig. 4), which is a standard value in our simulations. These approximations, however, are violated for large gain compression, $\varepsilon = 3 \cdot 10^{-22}$ m^3 (mustard dots in Fig. 4(a)). The scatter of dots is huge; the original dashed loop no longer confines the dots; the shifts of the dots and the solitary SL resonance deviate from the loop's diagonal.

In the presence of the nonvanishing ε, the shift of the solitary SL resonance and the zero-$\Im\Omega$ positions towards higher carrier densities is imposed by the approximate relation

$$
\begin{aligned}
2\Im\langle\beta_s\rangle &\approx g_T(\langle N_s\rangle, \varepsilon\langle|E|^2\rangle) - \alpha \quad \Rightarrow \\
\langle N_s\rangle &\approx N_{\text{tr}} + \frac{2\Im\langle\beta_s\rangle + \alpha}{g'}(1 + \varepsilon\langle|E|^2\rangle),
\end{aligned}
\tag{12}
$$

where $\Im\langle\beta_s\rangle$ is the (spatially-averaged) value of $\Im\beta$ needed for achieving the mode's threshold (i.e., vanishing of $\Im\Omega$) independently of the spatially averaged photon density $\langle|E|^2\rangle$ or the applied value of ε. Thus, an increase of $\varepsilon\langle|E|^2\rangle$ implies the growth of the averaged threshold density $\langle N_s\rangle$, which is depicted on the ordinate axis of Fig. 4. An increase of $\langle N_s\rangle$ and the nonvanishing α_{H} imply a corresponding angular frequency shift along the diagonal. For large ε, a perfect along-diagonal shift is violated since our model (3) assumes that $\Re\beta$ is independent of ε. Zero-$\Im\Omega$ positions represented by dots in Fig. 4 were calculated by exploring the CC and, when possible, the LFF states, where $\langle|E|^2\rangle$ shows significant fluctuations. Due to Eq. (12), we also got corresponding fluctuations of zero-$\Im\Omega$-defining $\langle N \rangle$, which are best visible for high values of ε.

Finally, Fig. 4(b) shows similar zero-$\Im\Omega$ calculations performed using small and moderate gain compression ε and different values of α_{H}. In all these cases, the red dots, calculated for $\varepsilon = 3 \cdot 10^{-24}$ m^3, are nicely located along the theoretical CCM loops, whereas the light blue dots obtained for $\varepsilon = 3 \cdot 10^{-23}$ m^3 show dislocations, discussed in panel (a) of this figure. In contrast to the $\alpha_{\text{H}} = 3.5$ case, the repetition rate of the LFF events for $\alpha_{\text{H}} = 5$ is higher, and the optical frequency band determined by all excited modes is about $(5/3.5)$ times larger than those presented in panel (a). A different situation was observed for small α_{H}. For $\alpha_{\text{H}} = 2$, we still could get a chaotically fluctuating CC regime, but without the evidence of the LFF, high $\langle N \rangle$, and, thus, without the involvement of modes with large frequency offsets. Finally, a few dots depicted in Fig. 4(b) in the case of $\alpha_{\text{H}} = 0$ represent only a few modes involving transients towards the steady state at the MGM.

5   Field expansion into optical modes

Let us now discuss the dynamically changing contributions of different modes to optical fields during the CC regime. For this reason, we analyzed the contributions of 1200 instantaneous modes $[\Theta_k(z), \Omega_k]$ during the above-mentioned 100-ns long transient simulations of the general TW model with $\kappa = 0.1$, $\alpha_H = 3.5$, and other parameters defined in Section 2. Calculated modes could fully cover the angular frequency range around the central solitary SL resonance. The field function $\Psi(z, t_0)$, propagation factor $\beta(z, t_0)$, corresponding eigenfunctions $\Theta_k(z)$, and Eq. (5) were used to find the mode amplitudes $f_k(t_0)$ at the sequence of about 25 ps separated time instants t_0.

For the standard case of $\varepsilon = 3 \cdot 10^{-23} \, \mathrm{m}^3$ (light blue dots in Fig. 4(a)), the results of our simulations for approximately one period of LFFs are summarized in Fig. 5. This figure reveals dynamics and mutual dependencies of (spatially averaged) carrier density $\langle N(t) \rangle$ and intensities $|f_j|^2$, angular frequency $\Re\Omega_j$, and damping $-2\Im\Omega_j$ of multiple modes and explains the origins of different mode beating frequencies that can be expected in the rf spectrum of much longer transients. To enable easy estimation of optical frequency separations, instead of the relative angular frequencies $\Re\Omega$ or ω, we depict relative frequencies $\nu = \Re\Omega/2\pi$ of the modes or $\omega/2\pi$ of the CCMs on the axes of the figure.
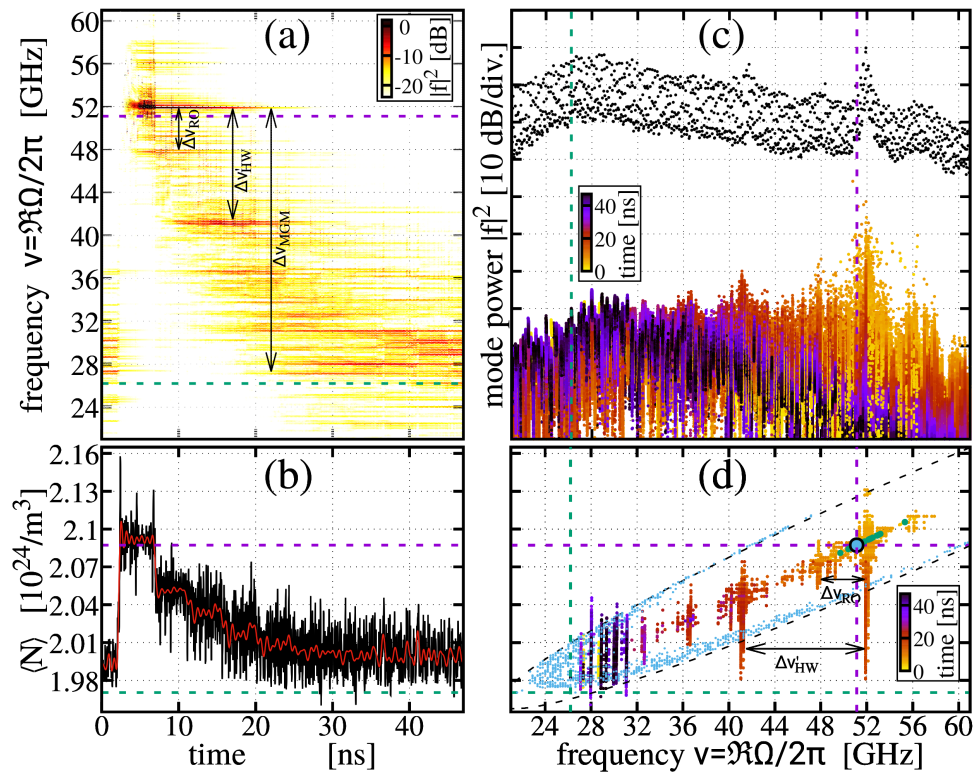

Figure 5: Mode analysis of the CC regime. (a): Color-coded intensities $|f_j|^2$ of all modes in the given spectral range during the 47 ns transient. (b): Corresponding (black) and low-pass filtered (red) time trace of $\langle N \rangle$. (c): Same as (a) with color-coding of time instants. Black dots: up-shifted time-averaged optical spectrum. (d): $(\nu, \langle N \rangle)$ of the modes when $|f(t)|^2 > -10$ dB [shown by red to black color in panel (a)]. Same color coding as in (c). Blue dots, black dashes, thick empty bullet, and green dots: the zero-$\Im\Omega$ positions, the CCM curve, the solitary SL resonance, as in Fig. 4, and $\sqrt{K_z} > 100$, respectively. Dashed lines: ν_{MGM}, N_{MGM} (green), and ν_{FP}, N_{FP} (magenta).

Sharing the same abscissa axis, panels (a) and (b) of Fig. 5 show the time evolution of different mode intensities (see the color coding) and the carrier density. The white-to-black color in Fig. 5(a)

represents intensities of different modes at given frequencies and time instants in the vicinity of one of several solitary SL resonances. All modes with substantial (red-to-black) intensity are confined within the frequency band, limited from below by ν_{MGM}, represented by the horizontal green dashed line. The upper limit of this band is just above ν_{FP} (dashed magenta), i.e., approximately at the frequencies where we could detect the EP and the exceptional mode in the simplified TW model; see Fig. 3(b) and the inset there. At $t \approx 2\,\mathrm{ns}$, $\nu \approx 52\,\mathrm{GHz}$ modes could quickly reach high-intensity levels, whereas ν_{MGM}-surrounding modes become damped. During the remaining time, the modes with smaller ν were gradually enhanced, whereas all but a single $52\,\mathrm{GHz}$ mode were quickly damped. We can recognize well-pronounced modes (or mode clusters) at about $\nu = 52$ and $41.5\,\mathrm{GHz}$, which could preserve significant intensities during prolonged time intervals and, thus, imply a signature of $\Delta\nu'_{\mathrm{HW}} \approx 10.5\,\mathrm{GHz}$ mode beating frequency in the rf spectrum. The existence of further multiple well-amplified modes at $\nu \approx 32$ GHz for $t \in [20, 35]$ ns and the interaction of these modes with still active $41.5\,\mathrm{GHz}$-modes further enhance $\Delta\nu'_{\mathrm{HW}}$ contributions to the rf spectrum.

The black curve in panel (b) shows the corresponding evolution of the spatially averaged carrier density, mainly fluctuating between N_{MGM} and N_{FP}, represented by dashed horizontal lines. A close inspection and an additionally performed low-pass filtering of $\langle N(t) \rangle$ [red curve in panel (b)] reveal that at the first part of the presented transient, carriers mainly evolve along several steps with an approximate length of $\tau = 4.5\,\mathrm{ns}$, where they oscillate with $\Delta\nu_{\mathrm{RO}} \approx 4\,\mathrm{GHz}$ frequency, which is a bit smaller than $\sim 5\,\mathrm{GHz}$ RO frequency of the solitary SL, see black spectra in Fig. 2(c). In Fig. 5(a), the signature of $\Delta\nu_{\mathrm{RO}}$-oscillations is represented by excited 56- and, especially, $48\,\mathrm{GHz}$-modes for $t \in [2, 15]$ ns, and by accordingly separated further high intensity modes or mode clusters (e.g., 37 and $41\,\mathrm{GHz}$ or 27 and $31\,\mathrm{GHz}$ modes) during nonvanishing time intervals. By comparing panels (a) and (b), one can recognize that the amplification or damping of one or another new group of modes in (a) correlates with the beginning and the end of these steps. In the second part of the trajectory, where the steps of $\langle N(t) \rangle$ can not be recognized anymore, multiple modes in the wide frequency band close to the MGM are excited. Simultaneous action of still not fully damped $52\,\mathrm{GHz}$-mode and already excited MGM at $t \approx 20$ ns is responsible for the $\Delta\nu_{\mathrm{MGM}}$-signature in the rf spectrum.

Fig. 5(d) again gives us the frequency-carrier density representation of the calculated trajectory. The dashed curve, blue dots, and empty bullet were already explained when discussing Fig. 4(a). The remaining small dots show positions (frequency $\nu(t)$ and carrier density $\langle N(t) \rangle$) of the modes which, at the related (color-coded) time instants, had large intensities $|f(t)|^2$ [corresponding to a red-to-black color in panel (a)]. Most of the modes further apart from the MGM could get large intensities only when $(\nu, \langle N \rangle)$ were located along the diagonal of the dashed (or blue-dot framed) loop where mode damping $\Im\Omega$ reaches the highest negative values for the given $\langle N \rangle$; see also discussion of Fig. 3(b). During the prolonged stay of $\langle N(t) \rangle$ at the upper step at about N_{FP} [panel (b)], several modes with ν just slightly exceeding ν_{FP} [panel (a)] had the largest possible amplification, i.e., the smallest possible $\Im\Omega$ [see the discussion of the red shaded region of Fig. 3(b)]. Notably, due to significant values of the $\sqrt{K_z}$ factor[3], which exceeded 100 at the green-dot indicated positions, the enhanced coupling of neighboring modes also contributed to the intensity exchange between the modes. After the descent of $\langle N(t) \rangle$ to the second step at about $\tilde{N}' = 2.05 \cdot 10^{24}\,\mathrm{m}^{-3}$, new modes at $\nu \approx 41.5\,\mathrm{GHz}$ corresponding to the smallest available $\Im\Omega(\tilde{N}')$ at the CCM-loop's diagonal are significantly amplified. Previously dominating exceptional mode and its neighbors at this new value of $\tilde{N}'$ still have $\Im\Omega \approx 0$, i.e., $(\nu_{\mathrm{EP}}, \tilde{N}')$ is approximately at zero-$\Im\Omega$ points, blue dots in Fig. 5(d). Thus, ω_{FP}-surrounding modes can preserve their intensity and produce $\Delta\nu'_{\mathrm{HW}}$-GHz beating with the newly amplified modes. $\tilde{N}'$ and $(\nu_{\mathrm{EP}}, \tilde{N}')$, after accounting for nonlinear gain compression induced up-shift of the zero-$\Im\Omega$ positions, can be nicely approximated by the simplified TW model-defined

---

[3]Typical values of $\sqrt{K_z}$ for $N \approx N_{\mathrm{MGM}}$ were between 1 and 3.

$N' = N_{FP} + \Delta N'$ (satisfying the second equation in (10)) and $(0, \Delta N')$ CCM, empty triangle in Fig. 3(b). Therefore, the above-discussed beating can be approximated by the half-width of the CCM curve at $\Delta N'$, $\Delta \nu'_{HW} \approx W(\Delta N')/4\pi$. The subsequent reduction of $\langle N(t) \rangle$ implies damping of the exceptional mode and its neighbors but, similarly as before, preserves the intensity of 41.5 GHz-range modes. At the end of the calculated transient (like at its beginning), only the modes at the lower part of the CCM loop have visible contributions.

Finally, panel (c) gives another optical-spectra-like presentation of the calculated transient. Like in panel (d), different colors of the dots represent time instants at which the mode intensities have been estimated. Panel (c) shows that the largest intensities achieved by the exceptional mode and its neighbors around $\nu = 52$ GHz were almost three orders higher than those at $\nu = 41.5$ GHz or around the MGM. However, these large intensities could be sustained only during the tiny time intervals since, due to the high K_z factor and the significant coupling between the modes at high-N levels, the mode intensity was transferred to the neighboring modes; see scattered dots with high $|f|^2$ values to the left and, especially right from ν_{EP}. Notably, the time-averaged optical spectrum obtained using the DFFT (see the discussion of Fig. 2(d)), black dots in Fig. 5(c), can satisfactorily represent the intensities $|f_k|^2$ of the most important modes, even though information about the huge instant peak values of the exceptional mode or the time subintervals where several modes or mode clusters have large amplitudes and are interacting, is lost. CCM separation in this representation is determined by approximately seven discrete angular frequency steps, which allows for resolving the averaged power of each individual mode and induces $\Delta \nu_{EC}$-periodic modulation of the spectral envelope.
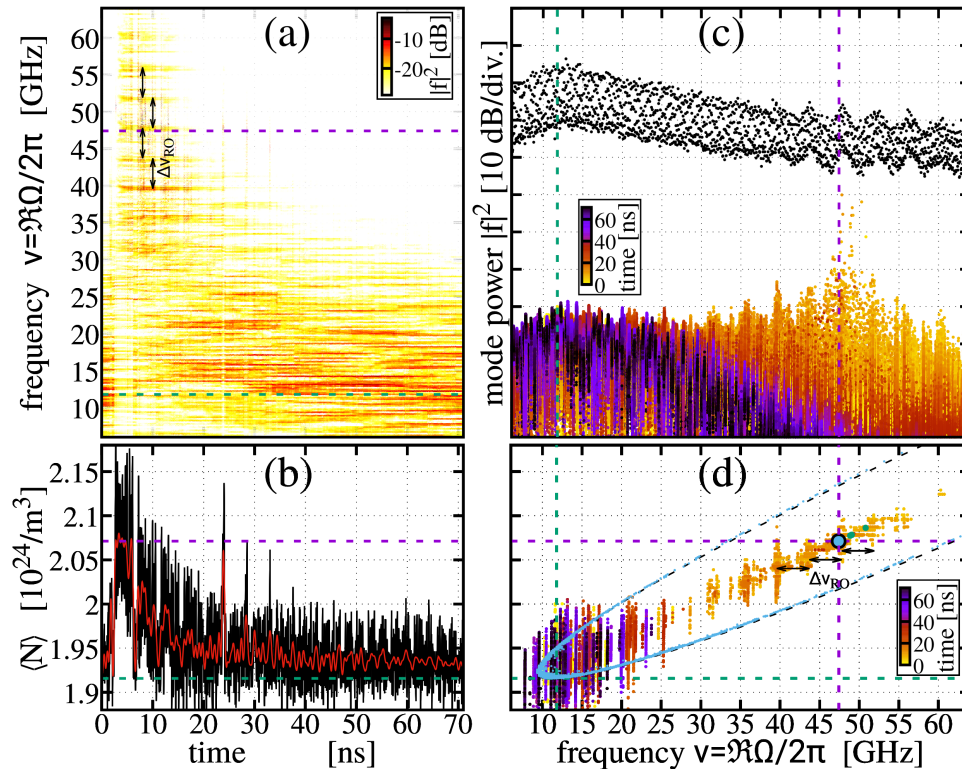

Figure 6: Mode analysis of the CC regime for $\varepsilon = 3 \cdot 10^{24}$ m^3 and $\kappa = 0.15$. All panels and notations as in Fig. 5.

Fig. 6 provides a similar representation of the simulations performed for $\kappa = 0.15$ and low gain compression, $\varepsilon = 3 \cdot 10^{-24}$ m^3. The considered 71 ns long transient here now represents a less regular separation between two LFF events. The decimation of the gain compression ε causes the

reduction of the RO damping, which implies increased amplitude fluctuation and the absence of the well-pronounced step-like descent of $\langle N(t) \rangle$ from the high N_{FP} values down to N_{MGM}, cf. panel (b) of Figs. 5 and 6. The reduced damping and increased fluctuation of $\langle N(t) \rangle$ prevent the formation of durable high-intensity mode clusters with $\Delta\nu'_{\mathrm{HW}}(\kappa)$-mode frequency separation in Fig. 6(a), such that a reduction of the rf spectral peaks at $\Delta\nu'_{\mathrm{HW}}(\kappa)$ and their enhancement at $\Delta\nu_{\mathrm{RO}}$ can be expected. The trajectory spends less time in the neighborhood of the solitary SL resonance and the EP during the LFF event, such that the contribution of the exceptional mode and its neighbors to time-averaged optical spectra is also reduced: cf. black dots in panel (c) of Figs. 5 and 6 close to the vertical dashed magenta lines. On the other hand, like in Fig. 5(d), the modes reach their largest intensities along the diagonal of the CCM curve or in the vicinity of the MGM, see Fig. 6(d).

In general, the presented mode analysis of the calculated transients in the LFF regime reminds the corresponding transitions reported in the LK model [12, 13, 14, 15], where the fast departure of the trajectory from the MGM surrounding and its slow return back was explained by the action of the unstable manifold of the saddle-type ECM, and the finite time τ spent by the trajectory in the vicinity of multiple node-type ECMs. In contrast, the mode analysis above only indirectly relies on the multiple CCM positions but considers changing contributions of the instantaneous mode amplitudes evolving according to Eq. (6). Our analysis has enabled us to identify modes capable of getting the largest amplification at certain quasi-steady levels of $\langle N \rangle$. In particular, the exceptional mode, which can reach the overall largest amplification rate, but also is responsible for sharing its power with the neighboring modes. Our mode analysis also provides a comprehensive time-frequency domain representation of the dynamic states of the SLDOF.

6   Discussion

In the examples of Section 5, we analyzed the dynamics of 1200 modes around a single solitary SL resonance during a 100 ns transient with about 25 ps time steps. Such mode analysis can quickly become too demanding of computational resources when consideration of μs-range transients, more extensive spectral ranges, and study of different parameters is required. For example, the above-performed analysis has required a Gigabyte of computer memory, more than 2-hour calculations, and an additional preselection of the initial time moment since the trajectory was reaching high values of $\langle N \rangle \approx N_{\mathrm{FP}}$ approximately once or twice in each 100 ns. This time range preselection is even more critical when the separation between the LFF events, which are the main reason for obtaining broadband rf spectrum, reaches several hundreds of nanoseconds at high κ. For comparison, a single $1\,\mu$s transient calculation can be done in about one minute without performing mode analysis. Thus, to characterize the dynamics of SLDOF systems when performing parameter scans, we still rely on direct numerical integration of model equations as we did when drawing Fig. 2, and use the mode analysis discussed above to better understand these simulations.

Let us again discuss the simulated spectral maps of Fig. 2 using information from the mode analysis. First, we apply a sliding averaging of the rf spectra using $\Delta\nu_{\mathrm{EC}}$-long windows. This filtering allows us to remove the periodically reappearing resonance peaks separated by $\Delta\nu_{\mathrm{EC}}$ from the spectral map of Fig. 2(a) for the purpose of showing the envelope of the rf spectrum. The resulting filtered maps for $\varepsilon = 3 \cdot 10^{-23}$ m^3 and $3 \cdot 10^{-24}$ m^3 are shown in Figs. 7(a) and (c), respectively. Panels (b) and (d) show the corresponding mapping of the optical spectra in the neighborhood of a single central solitary SL resonance wavelength $\Delta\lambda_{\mathrm{FP}}$, represented by the horizontal dash-dotted line. Solid and dashed white lines in these diagrams are κ-dependent frequency and wavelength offsets $\Delta\nu_{\mathrm{MGM}} = |\Delta\omega_{\mathrm{MGM}}/2\pi|$, $\lambda_0^2 \Delta\nu_{\mathrm{MGM}}/c$ and $\Delta\nu'_{\mathrm{HW}}$, $\lambda_0^2 \Delta\nu'_{\mathrm{HW}}/c$. In the moderate gain compression case, $\varepsilon = 3 \cdot 10^{-23}$ m^3,
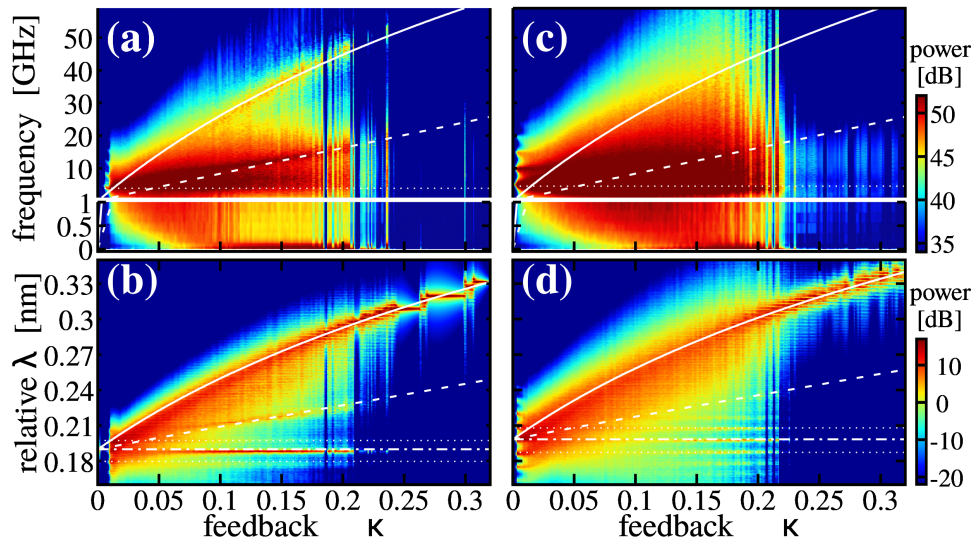
Figure 7: Mappings of the filtered rf (upper panels) and optical spectrum close to one of the solitary SL resonances (lower panels) for increased κ, color-coded on a dB scale, see also Fig. 2. $\varepsilon = 3 \cdot 10^{-23}\,\mathrm{m}^3$ in (a), (b) and $3 \cdot 10^{-24}\,\mathrm{m}^3$ in (c), (d), respectively. Solid, dashed, and dotted lines: $\Delta\nu_{\mathrm{MGM}}(\kappa)$, $\Delta\nu'_{\mathrm{HW}}(\kappa)$, and $\Delta\nu_{\mathrm{RO}}$ in (a) and (c), or corresponding wavelength shifts from $\Delta\lambda_{\mathrm{FP}}$ (dash-dotted line) in (b) and (d).

these lines can properly indicate the enhanced spectral peaks in the optical spectra, panel (b), and in the rf spectra, panel (a), for $\kappa \gtrsim 0.1$. When $\varepsilon = 3 \cdot 10^{-24}\,\mathrm{m}^3$, the MGM offsets (solid lines) can be used to define the main lasing wavelengths, panel (d), and approximate spectral bandwidth of the CC, panel (c). $\Delta\nu'_{\mathrm{HW}}$-defined estimates (dashed lines), however, totally fail to indicate distinguishable peaks in the spectral maps, which is due to the damping's reduction and is in agreement with the mode analysis presented in Fig. 6. In contrast, the RO-induced spectral peaks, dotted horizontal lines, are much more pronounced now, cf. panels (d) and (b) of Fig. 7. Since the gain compression in both cases was moderate or small, the compression-induced shift of the solitary SL resonance is also small (cf. dash-dotted lines in Figs. 7 (b) and (d)), and the theoretical CCM loops decently approximate the zero-damping positions (cf. light blue and red dots in Fig. 4). The comparison of panels (a) and (c) reveals that enhanced ε is preferable when looking for the MGM-defined steady states at high κ (see spectra of such stabilized case at $\kappa = 0.25$ in Fig. 2(c) and (d)). On the other hand, small ε is preferable when the CC regime with broad and more uniform rf spectra at moderate and high κ values is required. The results here-in connect well with prior experimental data [21, 22].

7 Conclusions

In conclusion, we analyzed the CC regime of the SLDOF system using the TW model and the analysis of instantaneous optical modes. We demonstrated how the mode analysis, in combination with direct simulations of the model equations, allowed us i) to get a comprehensive time-frequency characterization of the calculated chaotic transients, ii) analyze the relations between the carrier density dynamics and the amplification or damping of modes, iii) to identify simultaneously acting prominent modes or mode clusters responsible for the most pronounced mode beat frequencies in the emission's intensity, and iv) to find preferable changes in the model parameters desired for enhancing or reducing the feedback range suited for achieving the CC and the LFFs or increasing the CC rf band at fixed

feedback. We demonstrated that essential characteristics of the SLDOF, such as the rf bandwidth of the CC regime and key frequencies that show peaks in the rf power as seen in experimental systems can be accurately determined by fast calculations based on the analysis of the modes and the steady states in the simplified TW model. Further work on the boundaries of the LFF regions will be reported elsewhere. We have also found a correlation between the location of the exceptional point and the corresponding exceptional mode in the vicinity of each solitary SL resonance with the upper optical frequency bound in the CC regime. Further exploration of the exception point can lead to a better understanding of the complex dynamics in SLDOF and improve device designs suited for generating broad-band chaos, in particular.

References

[1] D. Kane and K. Shore, eds., *Unlocking Dynamical Diversity: Feedback Effects on Semiconductor Lasers* (John Wiley & Sons, 2005). doi: 10.1002/0470856211

[2] J. Ohtsubo, *Semiconductor Lasers: Stability, Instability and Chaos*, Springer Series in Optical Sciences (Springer, 2017), 4th ed. doi: 10.1007/978-3-319-56138-7

[3] M. Soriano, J. García-Ojalvo, C. Mirasso, and I. Fischer, "Complex photonics: Dynamics and applications of delay-coupled semiconductors lasers," *Reviews of Modern Physics* **85**, 422–470 (2013). doi: 10.1103/RevModPhys.85.421

[4] M. Zhang and Y. Wang, "Review on chaotic lasers and measurement applications," *J. Lightwave Tech.* **39**, 3711–3723 (2021). doi: 10.1109/JLT.2020.3043829

[5] H. Hasegawa, K. Kanno, and A. Uchida, "Parallel and deep reservoir computing using semiconductor lasers with optical feedback," *Nanophotonics* **12**, 869–881 (2023). doi: 10.1515/nanoph-2022-0440

[6] R. Lang and K. Kobayashi, "External optical feedback effects on semiconductor injection laser properties," *IEEE J. Quantum Electron.* **16**, 347–355 (1980). doi: 10.1109/JQE.1980.1070479

[7] M. Radziunas and H.-J. Wünsche, "Multisection lasers: Longitudinal modes and their dynamics," in *Optoelectronic Devices - Advanced Simulation and Analysis,* J. Piprek, ed. (Springer, 2005), chap. 5, pp. 121–150. doi: 10.1007/0-387-27256-9_5

[8] M. Radziunas, "Numerical bifurcation analysis of the traveling wave model of multisection semiconductor lasers," *Physica D: Nonlinear Phenomena* **213**, 98–112 (2006). doi: 10.1016/j.physd.2005.11.003

[9] R. Tkach and A. Chraplyvy, "Regimes of feedback effects in 1.5-μm distributed feedback laser," *IEEE J. Lightwave Technol.* **4**, 1655–1661 (1986). doi: 10.1109/JLT.1986.1074666

[10] S. Donati and R.-H. Horng, "The diagram of feedback regimes revisited," *IEEE J. Sel. Top. Quant. Electron.* **19**, 1500309 (2013). doi: 10.1109/JSTQE.2012.2234445

[11] D. Lenstra, B. Verbeek, and A. den Boef, "Coherence collapse in single mode semiconductor lasers due to optical feedback," *IEEE J. Quant. Electron.* **21**, 674–679 (1985). doi: 10.1109/JQE.1985.1072725

[12] J. Mork, B. Tromborg, and J. Mark, "Chaos in semiconductor lasers with optical feedback: theory and experiment," *IEEE J. Quant. Electron.* **28**, 93–108 (1992). doi: 10.1109/3.119502

[13] T. Sano, "Antimode dynamics and chaotic itinerancy in the coherence collapse of semiconductor lasers with optical feedback," *Phys. Rev. A* **50**, 2719–2726 (1994). doi: 10.1103/PhysRevA.50.2719

[14] G. van Tartwijk A.M. Levine and D. Lenstra, "Sisyphus effect in semiconductor lasers with optical feedback," *IEEE J. Sel. Topics Quantum Electron.* **1**, 466–472 (1995). doi: 10.1109/2944.401230

[15] B. Tromborg, J. Mork, and V. Velichansky, "On mode coupling and low-frequency fluctuations in external-cavity laser diodes," *Quantum and Semiclassical Optics* **9**, 831–851 (1997). doi: 10.1088/1355-5111/9/5/014

[16] M. Radziunas, "Traveling wave modeling of nonlinear dynamics in multisection semiconductor laser diodes," in *Handbook of Optoelectronic Device Modeling and Simulation: Lasers, Modulators, Photodetectors, Solar Cells, and Numerical Methods,* vol. 2 J. Piprek, ed. (CRC Press, 2017), chap. 31, pp. 153–182. doi: 10.4324/9781315152318-6

[17] J. Javaloyes and S. Balle, "Emission directionality of semiconductor ring lasers: a traveling-wave description," *IEEE J. of Quantum Electronics* **45**, 431–438 (2009). doi: 10.1109/JQE.2009.2014079

[18] M. Radziunas, "Calculation of the steady states in dynamic semiconductor laser models," *Optical and Quantum Electronics* **55**, 121 (2023). doi: 10.1007/s11082-022-04385-1

[19] M. Radziunas, D. Little, and D. Kane, "Numerical study of optical feedback coherence in semiconductor laser dynamics," *Optics Letters* **44**, 4207–4210 (2019). doi: 10.1364/OL.44.004207

[20] R. Ju, Y. Hong, and P. Spencer, "Semiconductor lasers subject to polarisation-rotated optical feedback," *IEE Proceedings Optoelectronics* **153**, 131–137 (2006). doi: 10.1049/ip-opt:20050049

[21] J. Toomey and D. Kane, "Mapping the dynamic complexity of a semiconductor laser with optical feedback using permutation entropy," *Optics Express* **22**, 1713–1725 (2014). doi: 10.1364/OE.22.001713

[22] D. Kane and M. Radziunas, "Chaos spectrum – semiconductor laser with delayed optical feedback," (2023). doi: 10.48550/arXiv.2312.14353

[23] M.-W. Pan, B.-P. Shi, and G. R. Gray, "Semiconductor laser dynamics subject to strong optical feedback," *Opt. Lett.* **22**, 166–168 (1997). doi: 10.1364/OL.22.000166

[24] K. Petermann, "Calculated spontaneous emission factor for double-heterostructure injection lasers with gain-induced waveguiding," *IEEE J. of Quantum Electron.* **15**, 566–570 (1979). doi: 10.1109/JQE.1979.1070064

[25] H. Wenzel, U. Bandelow, H.-J. Wünsche, and J. Rehberg, "Mechanisms of fast self pulsations in two-section DFB lasers," *IEEE J. of Quantum Electron.* **32**, 69–78 (1996). doi: 10.1109/3.481922

[26] M. Liertzer, L. Ge, A. Cerjan, *et al.,* "Pump-induced exceptional points in lasers," *Phys. Rev. Lett.* **108**, 173901 (2012). doi: 10.1103/PhysRevLett.108.173901

[27] J. Sieber, "Numerical bifurcation analysis for multisection semiconductor lasers," *SIAM J. on Appl. Dyn. Systems* **1**, 248–270 (2002). doi: 10.1137/S1111111102401746